Chapter 12
Applications of Viscoplasticity and Damage Models, the Thermomechanical Consistency and the Prospect of a Microstructural Representation

Matthias Ziegenhorn, Rainer Adelung, Rainer Franke, Robert Roszak, Ilja Sagradov, Daniela Schob, Holger Sparr, and Tomasz Kurzynowski

Abstract Material models in the framework of continuum mechanics cover the experimentally observed phenomena with a mathematical representation and a corresponding set of material parameters, which need to be established and validated. The theory of viscoplasticity plays an important role to describe the material behaviour of polymers and metals for a conventional as well as an additive manufacturing process. Naturally, the manufacturing process influences the microstructure and is to be reflected in the analysis and the characterisation of the material. The geometry reconstruction of microscopic images supports the extension of well-known material models and motivates the investigation of the interaction in bicontinuous composites. A universal measurement method as the contactfree thermography can be applied to validate the analytical assumption by an extended set of characteristics.

Key words: Viscoplasticity, Continuum damage mechanics, Porosity, Additive manufacturing, Thermomechanical consistency, Thermography, μComputed tomography, Image geometry reconstruction

Matthias Ziegenhorn · Rainer Franke · Robert Roszak · Ilja Sagradov · Daniela Schob · Holger Sparr
BTU Cottbus-Senftenberg, Universitätsplatz 1, 01968 Senftenberg, Germany,
e-mail: matthias.ziegenhorn@b-tu.de, rainer.franke@b-tu.de, robert.roszak@b-tu.de, ilja.sagradov@b-tu.de, daniela.schob@b-tu.de, holger.sparr@b-tu.de

Rainer Adelung
CAU Kiel, Kaiserstraße 2, 24143 Kiel, Germany,
e-mail: ra@tf.uni-kiel.de

Tomasz Kurzynowski
Politechnika Wrocławska, Wydział Mechaniczny, ul. Ignacego Łukasiewicza 5, 50-371 Wrocław, Poland,
e-mail: tomasz.kurzynowski@pwr.edu.pl

H. Altenbach et al. (eds.), *Material Modeling and Structural Mechanics*,
Advanced Structured Materials 161, https://doi.org/10.1007/978-3-030-97675-0_12

12.1 Introduction

The interest in describing complex material behaviour is ongoing and is fed by the development of new materials and their application in medical technology or automotive and aerospace engineering. These design materials should work safely and predictably until the defined end-of-life of the corresponding component or part. Material and damage models are developed at differentiated levels of abstraction and verified with adequate test procedures.

The fundamental model comparisons analysed by Krempl (1987) consider models applying a yield surface, e.g. Perzyna (1963) and Chaboche (1989), and models without using a yield surface, like in Bodner and Partom (1975). The application of these models is documented for metals in Olschewski (1996). The research on strain rate dependent models for elastic as well as plastic behaviour carried out by Reese (1998) justifies the attempt to capture the material behaviour of metals and polymers with the Chaboche or Bodner-Partom model.

Currently, the number of testing standards for additively manufactured polymers is limited. According to Forster (2015), only 20 of 47 available testing standards are conditionally applicable. This challenge adds up onto the constantly improved and modified manufacturing processes and an increased set of variable process parameters. The manufacturing process itself generates inhomogeneities on the microscale predominantly in form of voids. Under mechanical loading, a stress concentration in the vicinity of the voids occurs and, thus, a localized damage evolution is initiated. With the assumption of a statistically uniform void distribution and restrictions on the void properties, the original material models can be enhanced by ideas from the continuum damage mechanics, where ductile damage, referencing void initiation, growth and coalescence, can be represented by the models of Gurson (1977) or Lemaître and Desmorat (2005).

The generalised classification of material behaviour according to Haupt (2002) is used. The tensorial formulations of backstress, overstress and equilibrium stress developed by Haupt are applied and reference is made to the presentation of these variables in connection with the arguments related to dislocation movement and velocity in Krempl (1987).

To substantiate the material classification and to assess the suitability of the chosen modelling approach, a temperature evolution is very sensitive to certain deformation mechanisms. The required accuracy in the temperature measurement is given by modern infrared cameras. The pioneering works of Taylor and Quinney (1934); Oldyrev and Tamuzh (1969); Chrysochoos (2012) concerning a temperature evolution due to mechanical loading and the accompanying experimental methods for metallic and polymer materials have been initiating new thermomechanical modelling approached over the last decades. The fundamental KELVIN effect can be used to determine the yield point, while the dissipative phenomena for inelastic deformation or the microstructural evolution in cyclic loading becomes clearly evident for self-heating. The principles of continuum thermomechanics generate a universal framework for the formulation of thermodynamically consistent material models not limited to certain material classes and also provided the functionality for incor-

porating scale effects. The here considered models (Bodner and Lindenfeld, 1995; Bröcker and Matzenmiller, 2013; Kamlah and Haupt, 1998) are applied to casted and additively manufactured metal alloys with respect to plastic and viscoplastic deformation processes, where microstructural effects in terms of a material phase interaction are not in focus.

Complex material configurations due to strengthening, weakening or functional integration by particles require the representation of inhomogeneity. The analysis of models using representative volume elements (RVE) at the appropriate scale are very successful in this respect. Following the Eshelby approach for elastic material, Yanase et al. (2020) investigate the influence of the particle shape on the overall stiffness properties of a two-phase composite. A multi-step method proposed by El Ghezal and Doghri (2018) combines of the Eshelby-based Mori-Tanaka method, the generalized self-consistent scheme and the Gurson model to account for plastic deformations and a concurrent porosity evolution. A random dispersion of elastic spheres in an elastic-plastic polymer matrix is the subject of the FE-based numerical homogenisation by Khdir et al. (2013), where the statistical deviation was quantified with respect to the number of particles per control volume. Examples for bicontinuous material configuration (two interpenetrating phases) and a corresponding homogenised representation are given in Carolan et al. (2015); Soyarslan et al. (2019) and address three-dimensional networks within a matrix as in Arndt et al. (2021).

In this contribution, the addressed topics are reflected in the three main sections. Sect. 12.2 focuses on classical, viscoplastic material models in conjunction with continuum damage mechanics. An external temperature load is incorporated. The self-heating phenomenon is the core of Sect. 12.3. Especially, the extended evaluation of the thermomechanical process is pointed out, and the significance of the applied models is emphasized. In Sect. 12.4, the beginning of the analysis of bicontinuous or multiphase materials is shown by a model generation technique through microscopic image data processing, where the aforementioned procedures can be applied to.

12.2 Experimental and Numerical Investigation of Temperature-dependent Mechanical Behaviour of 3D Printed Polyamide 12

The engineering requirements for additively manufactured polymer components are growing as well as their applications are becoming more complex. Therefore, the additively manufactured polymers are increasingly used in mechanically stressed components. To ensure that additively manufactured polymers can withstand the new conditions, it is essential to subject them to a testing procedure.

It cannot be assumed that a homogeneous material structure is achieved in additive manufacturing in contrast to conventionally manufactured injection-molded components. The thermoplastic polyamide 12 (PA12) is one of the materials used and the subject of the described analysis. The damage behaviour under quasi-static

tensile stress and the relaxation properties are of special interest in the characterisation procedure.

12.2.1 Experimental Analysis

12.2.1.1 Sample Preparation

The samples have been prepared by selective laser sintering (SLS). The SLS PA2200 material has been used. A sPro 230 printer from 3D Systems with a power of 70 W was used. It was operated with a laser scanning speed of 10 m/s for the infill and 5 m/s for contours. The nominal layer thickness was 0.08 – 0.15 mm. The temperature of the pressure chamber and the process were 170 °C and 200 °C. The spherical powder particles had a size in the range of 20 – 80 µm. Due to the fact that no test standards exist for additive manufactured (AM) polymers, the geometry of the test specimens was chosen according to DIN EN ISO 527-2 Type 1A (DIN Deutsches Institut für Normung e.V., 2012), **Fig. 12.1**a. In previous investigations, it was found that the material properties only slightly depend on the printing direction (Franke et al., 2017). Therefore, all samples were printed in x-direction, according to the definition in **Fig. 12.1**b.

12.2.1.2 Test Conditions

Exhibiting PA12 at a temperature from 10 to 40 °C shows a significant influence on the mechanical properties. Therefore, three different types of tests were performed - (I) isothermal and (II) non-isothermal tensile tests and (III) isothermal multirelaxation tests. A servo-hydraulic test machine from ZwickRoell with a 25 kN load cell and temperature chamber were used. (I) For the isothermal tensile tests four levels of chamber temperature, 10 °C, 20 °C, 30 °C and 40 °C were selected. Five tests were carried out for each temperature level with a displacement rate of 0.5 mm/min, **Fig. 12.2** (*a*). (II) Five non-isothermal tests were performed with the temperature

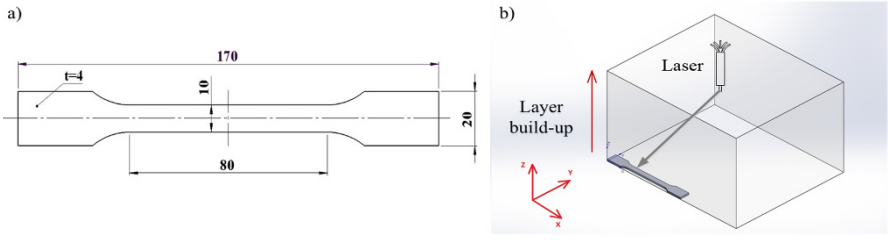

Fig. 12.1: (*a*) Dimensions of the specimen, (*b*) Sketch of the printing job: individual layers printed in xy-plane; the build-up (stacking direction) in z-direction.

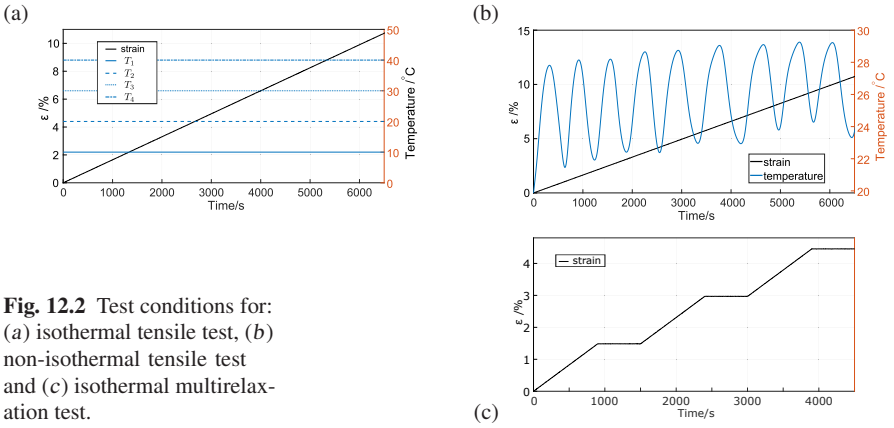

Fig. 12.2 Test conditions for: (*a*) isothermal tensile test, (*b*) non-isothermal tensile test and (*c*) isothermal multirelaxation test.

cyclically changing between $10-40\,^{\circ}\mathrm{C}$ at a rate of $0.2\,^{\circ}\mathrm{C/s}$ during tensile loading, **Fig. 12.2** (*b*). (III) Multirelaxation tests were built up stepwise and divided into three holding times and three tensile load steps. The holding times were 4 min and the displacement rate of the tensile load was kept constant during the test at 5 mm/min, **Fig. 12.2** (*c*).

12.2.2 Microanalysis

12.2.2.1 Scanning Electron Microscopy

To describe the damage behaviour, the microstructure of the fracture surfaces of the specimens was examined by means of a scanning electron microscopy (SEM) after the tensile tests, **Fig. 12.3**. The images show an inhomogeneous microstructure containing pores. In the fringe area, it was found that the printing process does not produce a smooth surface and that small notches are formed on the surface.

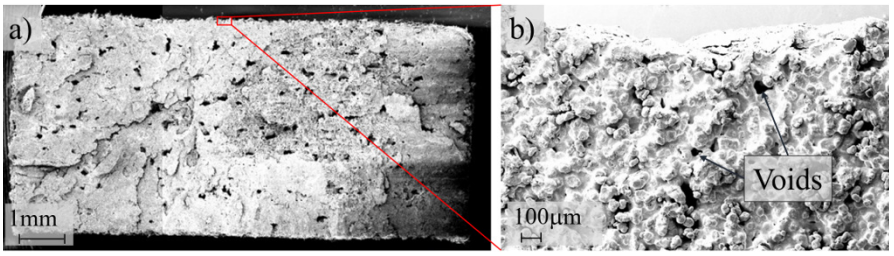

Fig. 12.3: Scanning electron micrographs, (*a*) fracture surface 40× magnification, (*b*) Section of the upper edge area, 150× magnification.

12.2.2.2 X-ray Computed Tomography

Figure 12.4 shows the reconstructed computed tomography (CT) images of a specimen at a virgin state and after tensile loading. A porosity of 3.7% for the virgin state resp. 3.6% for the loaded sample was measured. The distribution of the cavities over the specimen is very uniform, which means that an intensified melting on the surfaces and edges during the printing process did not take place.

A statistical uniform void distribution together with the average void size suggests that the assumption of material homogeneity and the validity of the phenomenological approach are justified.

12.2.3 Numerical Analysis

Previous investigations (Schob et al., 2019) have shown that additively manufactured PA12 behaves viscoplastically. The viscoplastic models established in recent years can essentially be divided into two groups. One group introduces a specific yield limit, while the other renounces an explicit yield limit and, consequently, a pure elastic domain altogether. The first group includes the material model of Chaboche (1989) and the material model of Bodner and Partom (1975); Bodner (2000) belongs to the second group.

A separated temperature dependency for each material parameter can be established for a temperature range of interest. A complete map involving a interdependence of all relevant parameters is usually experimentally out of scope. Instead, the Johnson-Cook approach allows a generalised covering of the temperature dependency in a material model and is mathematically applicable to the models of Bodner-Partom and Chaboche (Bodner, 2000; Cook and Cook, 1983).

Furthermore, the microstructure analysis in Schob et al. (2019) showed a porosity of 4.7% in the virgin samples. The pores have a spherical shape and change the shape during loading. To model the damage behaviour of PA12, the Gurson-Tvergaard-Needleman (GTN) model was successfully applied in Schob et al. (2019, 2020) for static and cyclic loading at room temperature.

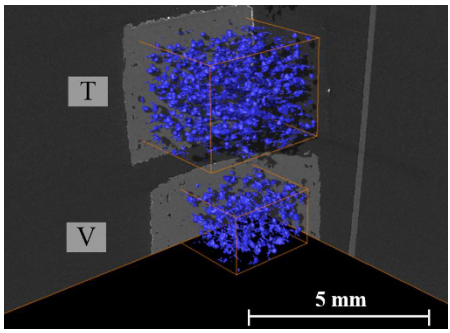

Fig. 12.4 CT rendering of pores for a virgin (V, bottom) and a loaded (T, top) specimen.

The Gurson (1977) and Lemaître and Desmorat (2005) damage models are the most commonly used approaches for simulating processes with ductile fracture. The approach of Lemaitre is based on the model of effective stresses by Kachanov (1980). In the initially two-dimensional formulation, Lemaitre derives the damage value from the ratio of the pore area fraction to the total area. The Gurson model was developed on the studies of void growth by Rice and Tracey (1969) and takes the void volume fraction of the total volume for the damage evolution into account.

In the following paragraphs, the Chaboche and the Bodner-Partom material models as well as the Johnson-Cook extension and the damage models of Gurson-Tvergaard-Needleman and Lemaitre are described. Furthermore, they are applied to the additively manufactured PA12 samples with the previously outlined loading schemes.

12.2.3.1 The CHABOCHE Model

The CHABOCHE model is composed as a system of differential equations. Considering the theory of infinitesimal deformation, the total strain rate $\dot{\boldsymbol{\varepsilon}}^{\mathrm{tot}}$ follows the additive split into an elastic $\dot{\boldsymbol{\varepsilon}}^{\mathrm{el}}$ and a viscoplastic $\dot{\boldsymbol{\varepsilon}}^{\mathrm{vp}}$ rate fraction,

$$\dot{\boldsymbol{\sigma}} = \mathbb{C} \cdot \left(\dot{\boldsymbol{\varepsilon}}^{\mathrm{tot}} - \dot{\boldsymbol{\varepsilon}}^{\mathrm{vp}} \right) \tag{12.1}$$

with the CAUCHY stress $\boldsymbol{\sigma}$ and the linear elastic stiffness tensor $\mathbb{C}$. Here, the definition of the viscoplastic strain rate $\dot{\boldsymbol{\varepsilon}}^{\mathrm{vp}}$ is decisive:

$$\dot{\boldsymbol{\varepsilon}}^{\mathrm{vp}} = \dot{\lambda} \frac{\partial \phi}{\partial \boldsymbol{\sigma}} \quad \text{with} \quad \lambda = \left\langle \frac{\phi}{K} \right\rangle^{n} \tag{12.2}$$

with the viscosity factor K and n. The viscoplastic multiplier λ describes the evolution of the viscoplastic deformation increment. The flow function ϕ enables the determination whether the material undergoes a pure elastic or an elastic-viscoplastic deformation (in the elastic domain $\phi < 0$; in the elastic-viscoplastic domain $\phi = 0$). The following equation defines the flow function, where σ^{y} is the yield stress and q_1, q_2 are the damage parameters according to Tvergaard and Needleman (1984).

$$\phi = \left(\frac{\sigma_{\mathrm{eq}}^{\mathrm{eff}}}{\sigma^{y}} \right)^{2} + 2 q_1 f^{*} \cosh \left(\frac{3 q_2}{2} \frac{\sigma_{\mathrm{m}}^{\mathrm{eff}}}{\sigma^{y}} \right) - 1 - (q_1 f^{*})^{2} \geqslant 0 \tag{12.3}$$

Furthermore, the flow function is defined by the effective stress $\sigma_{\mathrm{m}}^{\mathrm{eff}}$ and the VON MISES equivalent stress $\sigma_{\mathrm{eq}}^{\mathrm{eff}}$,

$$\sigma_{eq}^{eff} = \sqrt{\frac{1}{2}\left[(\sigma_1^r - \sigma_2^r)^2 + (\sigma_2^r - \sigma_3^r)^2 + (\sigma_3^r - \sigma_1^r)^2\right]} \tag{12.4}$$

$$\sigma_m^{eff} = \left(\frac{\sigma_{kk}^r}{3}\right) \tag{12.5}$$

$$\boldsymbol{\sigma}^r = \boldsymbol{\sigma} - \boldsymbol{\alpha}^* \tag{12.6}$$

$$\boldsymbol{\alpha}^* = (1 - f^*) \sum_{k=1}^{2} \boldsymbol{\alpha}^{(k)} \tag{12.7}$$

where $\boldsymbol{\sigma}^r$ is the relative stress and f^* the damage evolution. Compared to the previous investigation (Schob et al., 2019), the kinematic hardening $\boldsymbol{\alpha}^*$

$$\boldsymbol{\alpha}^* = T^h (1 - f^*) \sum_{k=1}^{2} \boldsymbol{\alpha}^{(k)} \quad \text{with} \quad k = 1, 2 \tag{12.8}$$

was extended by the Johnson-Cook equation T^h, Cook and Cook (1983); Bodner (2000). This approach takes into account the displacement of the flow surface due to the influence of temperature change. The Johnson-Cook equation is defined as,

$$T^h = \left(1 - \frac{T - T^0}{T^m - T^0}\right)^d \tag{12.9}$$

by the empirical value d and the melting temperature T^m, with ($T \geqslant T^0$). For the isothermal experiments T^h equals to one. In Eq. (12.8), the kinematic hardening $\boldsymbol{\alpha}^{(k)}$ is defined by the following equation,

$$\dot{\boldsymbol{\alpha}}^{(k)} = \frac{2}{3} C^{(k)} \dot{\boldsymbol{\varepsilon}}^{vp} - \gamma^{(k)} \boldsymbol{\alpha}^{(k)} \dot{\varepsilon}_M^{vp} \quad \text{with} \quad k = 1, 2 \quad \text{and} \quad \dot{\varepsilon}_M^{vp} = \frac{\boldsymbol{\sigma}^r \dot{\boldsymbol{\varepsilon}}^{vp}}{(1 - f^*)\sigma^y} \tag{12.10}$$

where C and γ are hardening parameters and $\dot{\varepsilon}_M^{vp}$ is the rate of the equivalent viscoplastic strain.

12.2.3.2 The BODNER-PARTOM Model

The BODNER-PARTOM model has been used for modelling the mechanical behaviour of metals (Olschewski, 1996) and polymers (Zaïri et al., 2005). In contrast to the CHABOCHE model, it contains no formulation of an established yield criterion (Bodner, 2000). Thus, plastic deformation occurs at any time on the load-path, no matter whether loading or unloading takes place. The BODNER-PARTOM model is a system of ordinary first order differential equations and can be decomposed into an equation for the viscoplastic strain rate $\dot{\varepsilon}^{vp}$, the multiplier $\dot{p}$ connecting the strain rate with the stress deviator, the scalar variable Z_I representing isotropic hardening,

the tensorial variable $\mathbf{Z}_D$ representing kinematic hardening as well as the evolution equation for the inelastic work W^{vp}.

Here, the isotropic hardening variable Z_I consists of the coefficient for isotropic hardening m_1, the initial value for isotropic hardening K_0, the limiting (maximum) value for isotropic hardening K_1, the fully recovered (minimum) value for isotropic hardening K_2, the recovery rate coefficient for isotropic hardening A_1 and the recovery exponent for isotropic hardening r_1. The tensorial variable $\mathbf{Z}_D$ combines the coefficient for kinematic hardening m_2, the limiting (maximum) value for kinematic hardening K_3, the recovery rate coefficient for kinematic hardening A_2 and the recovery exponent for kinematic hardening r_2. The BODNER-PARTOM model is summarized in Eqs. (12.11) - (12.15).

$$\dot{\boldsymbol{\varepsilon}}^{vp} = \frac{3}{2}\dot{p}\frac{\boldsymbol{\sigma}'}{J(\boldsymbol{\sigma}')} \quad \text{with} \quad \boldsymbol{\sigma}' = \boldsymbol{\sigma} - \sigma_{ii}\mathbf{I} \tag{12.11}$$

$$\dot{p} = \frac{2}{\sqrt{3}}D_0 \exp\left[-\frac{1}{2}\left(\frac{Z_I + \mathbf{Z}_D \cdot \dfrac{\boldsymbol{\sigma}}{J(\boldsymbol{\sigma})}}{J(\boldsymbol{\sigma}')}\right)^{2n}\right] \tag{12.12}$$

Isotropic hardening

$$\dot{Z}_I = m_1(K_1 - Z_I)\dot{W}^{vp} - A_1\left(\frac{Z_I - K_2}{K_1}\right)^{r_1} \tag{12.13}$$

Kinematic hardening

$$\dot{\mathbf{Z}}_D = m_2\left(K_3\frac{\boldsymbol{\sigma}}{J(\boldsymbol{\sigma})} - \mathbf{Z}_D\right)\dot{W}^{vp} - A_2\left(\frac{\frac{2}{3}J(\mathbf{Z}_D)}{K_1}\right)^{r_2}\frac{\mathbf{Z}_D}{J(\mathbf{Z}_D)} \tag{12.14}$$

Specific viscoplastic work rate

$$\dot{W}^{vp} = \boldsymbol{\sigma} \cdot \dot{\boldsymbol{\varepsilon}}^{vp} \tag{12.15}$$

12.2.3.3 The GURSON-TVERGAARD-NEEDLEMAN model

Since the CT results (Schob et al., 2019) suggest assuming spherical pores, the GTN model (Tvergaard and Needleman, 1984) was applied. The original Gurson model from 1977 is based on the assumption of spherical pores (Gurson, 1977). Whereby a rigid-perfect plastic material behaviour is accepted and the flow criterion of VON MISES is applied. A constant strain rate is applied. The flow function ϕ (Eq. (12.3)) is defined as a function of the macroscopic stress and the randomly distributed void

volume. Tvergaard and Needleman (1984) extended the Gurson model. The extended model considers growth, nucleation and coalescence.

With the modified void volume fraction f^*, it is now possible to model the load capacity loss above a critical void volume fraction f_c. When a critical void volume fraction f_c is reached, coalescence occurs. This process continues until a failure value f_F is reached and the specimen fails. The initial porosity f_0 is determined at time $t = 0$.

$$f^* = \begin{cases} f_0 & \text{if} \quad t = 0 \\ f & \text{if} \quad f \leqslant f_c \\ \dfrac{1}{q_1} - f_c & \\ f_c + \dfrac{\frac{1}{q_1} - f_c}{f_F - f_c}(f - f_c) & \text{if} \quad f_c < f \leqslant f_F \end{cases} \tag{12.16}$$

The void volume fraction considers the growth f_g and nucleation f_n of voids, Eqs. (12.17) - (12.20).

$$\dot{f} = \dot{f}_g + \dot{f}_n \tag{12.17}$$

$$\dot{f}_g = (1 - f)\dot{\boldsymbol{\varepsilon}}^{vp}_{kk} \tag{12.18}$$

$$\dot{f}_n = \frac{f_N \dot{\bar{\varepsilon}}^{vp}}{S_N \sqrt{2\pi}} \exp\left(-\frac{1}{2}\left(\frac{\bar{\varepsilon}^{vp} - \varepsilon_N}{S_N} \right)^2 \right) \tag{12.19}$$

$$f_0 = f(t = 0) \tag{12.20}$$

Nucleation is controlled by the nucleation porosity f_N, the effective viscoplastic strain $\bar{\varepsilon}^{vp}$, the viscoplastic strain rate $\dot{\bar{\varepsilon}}^{vp}$, the mean strain ε_N and the standard deviation of the stress S_N. The GTN model contains 8 damage parameters. The initial damage parameter f_0 was determined by computed tomography in Schob et al. (2020) and is 4.7%.

12.2.3.4 The LEMAITRE Damage Model

Layered building of components in AM results in anisotropy and material defects, e.g. microcracks. Recent research (Stichel et al., 2017) revealed the correlation between microcracks in AM materials and anisotropy. Therefore, the focus of this work is the mathematical description of the microcracks.

The anisotropic mechanical response could be the direct result of distinct pore shapes or arrangements since pores are analogous to small pre-existing cracks (Stichel et al., 2017). 3D printed PA12 shows distinct brittle material behaviour in contrast to PA12 manufactured by injection moulding (Franke et al., 2017). The issue of brittleness should be addressed considering two features: first, the nucleation of a crack, which is favoured by the residual voids due to incomplete sintering; secondly the crack propagation (Dupin et al., 2012). If the material does not fully consolidate, crack initiation and failure can occur. (van Hooreweder et al., 2010) performed fatigue tests on laser sintered PA12 and found that the crack initiation

resulted from inclusions in the material caused by unfused powder particles. As a result, lower density parts had a higher chance of crack initiation and undergoing fatigue damage (Goodridge et al., 2012). The material density is a crucial influence factor for the fatigue life of the components. The lower the density, the more unfused powder particles appear and the higher the chance for crack initiation to start will be.

To predict rupture of structures with good accuracy, it is necessary to use coupled constitutive equations. Therefore, the viscoplastic model of BODNER-PARTOM is coupled with the LEMAITRE damage model (Lemaître and Desmorat, 2005). It is based on the concept of effective stress due to material damage and fatigue. The damage is caused by micro-cracks and only determined by the state in one single material point. So, the impact of damage nearby is not considered. A macro-crack is then considered as the set of points for which the local damage has reached its critical value at failure. The Lemaitre model has the form of a system of ordinary first order differential equations and can be decomposed into the effective stress rate $\dot{\sigma}_{\mathrm{eff}}$, the damage rate $\dot{D}$ and energy release rate Y. The damage rate consists of the elastic modulus E, the damage parameters s and S, as well as of the rupture time t_r. The LEMAITRE damage model for the one-dimensional case is given in Eqs. (12.21) - (12.24).
Effective stress

$$\dot{\sigma}_{\mathrm{eff}} = (1-D)E(\dot{\varepsilon} - \dot{\varepsilon}^{vp}) \tag{12.21}$$

Damage rate

$$\dot{D} = \left(\frac{Y}{S}\right)^{s} \dot{p} \tag{12.22}$$

$$S = \frac{(2s+1)^{\frac{1}{s}}}{2E} \left(\int_0^{t_r} \sigma_{\mathrm{eff}}^{2s}\, \dot{p}\, dt\right)^{\frac{1}{s}} \tag{12.23}$$

Energy release rate

$$Y = \frac{\sigma_{\mathrm{eff}}^2}{2(1-D)^2 E} \tag{12.24}$$

Further explanations on the LEMAITRE damage model can be found in Lemaître and Desmorat (2005). For simplicity reasons, only isotropic material damage was considered.

12.2.4 Results

The material model parameters were optimized by the nonlinear least square method. This method is commonly used for obtaining material parameters of the CHABOCHE viscoplastic material model (Gong et al., 2010). The solution of the equations of the material models with optimal material parameters is then compared with experimental results. In **Fig. 12.5** the results of the isothermal tensile test are presented and validated with the CHABOCHE-GTN model. Throughout all temperature stages an excellent agreement between experiment and simulation could be achieved. A direct dependency between temperature and the elastic modulus could be observed. The higher the temperature, the lower the elastic modulus. Furthermore, a decrease of the maximum stress with increasing temperature could be noticed.

In **Fig. 12.6** the results of the non-isothermal tensile test are presented and validated with the CHABOCHE-GTN-JC model. An excellent agreement between ex-

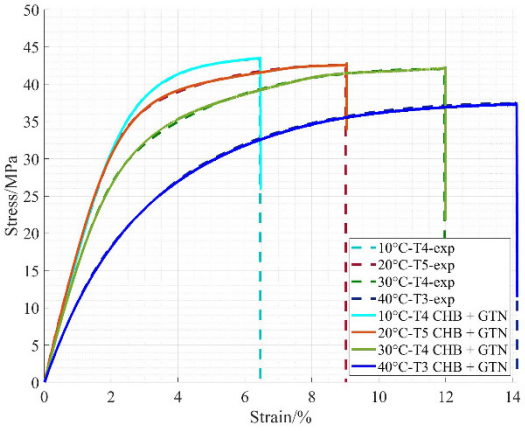

Fig. 12.5 Results of the isothermal tensile test, validation with the CHABOCHE-GTN model.

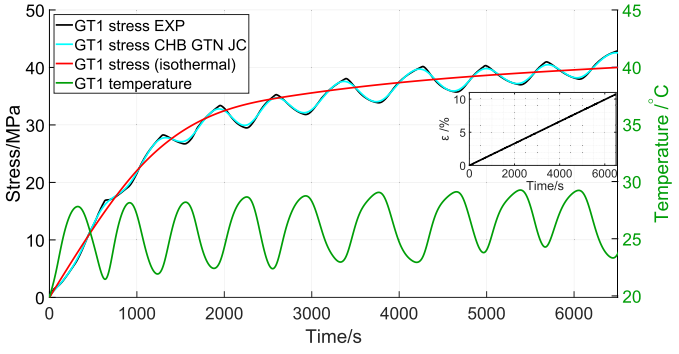

Fig. 12.6: Results of the non-isothermal tensile test, validation with the CHABOCHE-GTN-JC model.

periment and simulation could be achieved. The JOHNSON-COOK extension of the Chaboche-GTN model causes a stress increase with falling temperature and a stress decrease with growing temperature. So, the JOHNSON-COOK extension allows to precisely depict stress hardening and softening.

In **Fig. 12.7** the results of the multirelaxation test are presented and validated with the BODNER-PARTOM model as well as with the LEMAITRE micromechanical damage extension. The solution of the equations of the material models with optimal material parameters is compared with experimental results using the absolute deviation (Agius et al., 2017). It reproduces the discrepancy between measured and calculated stress of the material model at each time step of the experiment. An excellent agreement between experiment and simulation could be achieved with both approaches, but the extended model reached a slightly lower absolute deviation and thus a more realistic depiction of the material behaviour. This is due to consideration of the effective stress due to damage of the LEMAITRE micromechanical damage extension.

12.3 Thermomechanical Approach

In contrast to the described phenomenological description in the framework of continuum mechanics with the assumption of decoupling the mechanical and the thermal process, this section provides the full set of equations in terms of continuum thermomechanics towards a thermomechanical consistent material model. In this scheme, the second law of thermodynamics leads to the well-known COLEMAN-NOLL procedure motivating constitutive assumptions and the equation of heat conduction, as a major result of the energy balance, which is integrated in the set of equations to solve. Therefore, the applied load and the corresponding deformation path is understood as a thermodynamic process, which is expressed in a fully coupled thermomechanical problem and implies a temperature evolution in the specimen.

In this respect, the thermomechanical approach opens up the observation methods in the experimental analysis to the evolving temperature field of the samples and extents the classical characterisation procedure.

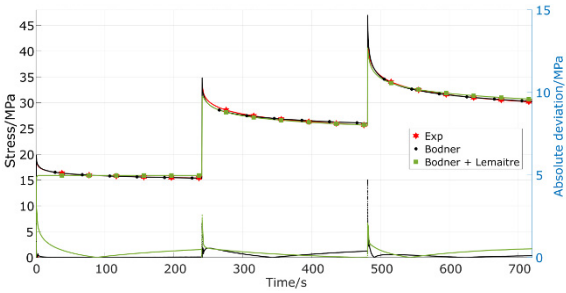

Fig. 12.7 Results of the multirelaxation test, validation with the BODNER-LEMAITRE model.

The central stress-strain characteristics are accompanied by the temperature evolution and the evolution of derived quantities such as the energy resp. energy-rate transformation ratio (ETR). These three characteristics combined can improve the assessment of the investigated deformation load path qualitatively as well as quantitatively.

The initial boundary value problem of the coupled displacement and temperature fields is experimentally well supported by a high-resolution infrared camera. A reduced thermal boundary value control simplifies the experimental measures to be realised. It is shown in the analysis that the attained surface temperature accuracy is well-suited for the identification of model parameters related to dissipative deformation phenomena.

12.3.1 Analytical Formulation in the Framework of Continuum Thermomechanics

As the analytical foundation for the description of deformation processes of fluids and solids in the framework of thermodynamics was initiated among others by the contributions of Truesdell and Noll (1992) in the 1960ies. Numerous valuable books and articles followed. A more recent book by Haupt (2002) collects the earlier findings in a clear systematisation and notation and addresses the theory of materials and its applicability to generalized material classes with a large set of various deformation phenomena comprehensively.

Thermodynamic consistency is proven by the fulfillment of the second law of thermodynamics, which can be rewritten by the reduced dissipation inequality of eq. (12.25).

$$\delta = \frac{1}{\rho}\boldsymbol{\sigma}\cdot\dot{\boldsymbol{\varepsilon}}^{\mathrm{i}} - \frac{\partial\hat{\psi}}{\partial\boldsymbol{\alpha}}\cdot\dot{\boldsymbol{\alpha}} - \frac{1}{\rho\theta}\mathbf{q}\cdot\mathbf{g} \geqslant 0 \quad \text{with} \quad \psi = \hat{\psi}\left(\boldsymbol{\varepsilon}^{e},\theta,\boldsymbol{\alpha}\right), \qquad (12.25)$$

$$\mathbf{g} = \boldsymbol{\nabla}\theta \quad \text{and} \quad \mathbf{q} = -\mathrm{k}\mathbf{g}\,.$$

The reduced dissipation inequality is the result of the COLEMAN-NOLL procedure, which connects the HELMHOLTZ free energy with the CAUCHY stress tensor $\boldsymbol{\sigma}$ as well as with the entropy designated by η in the next equation. Here, the thermodynamic potential of the HELMHOLTZ free energy ψ depends on the elastic fraction of the total strain, the temperature θ and a set of internal variables of tensorial and/or scalar type represented by $\boldsymbol{\alpha}$. The notation above incorporates the theory of infinitesimal deformation ($\boldsymbol{\varepsilon} = \boldsymbol{\varepsilon}^{e} + \boldsymbol{\varepsilon}^{\mathrm{i}}$ – additive decomposition of the strain tensor into an elastic resp. inelastic strain fraction) as well as the concept of internal variables $\boldsymbol{\alpha}$ to formulate the inelastic deformation phenomena. The temperature gradient is defined by $\mathbf{g}$ and forms by being multiplied with the thermal conductivity k the heat flux $\mathbf{q}$ – the isotropic case of FOURIER's law.

Then, the mechanical fraction, the first and second term in (12.25), of the internal dissipation δ consists of the plastic stress power and the rate of stored energy dominated by the evolution of the internal variables assembled in α.

The thermodynamic restrictions lead to the GIBBS equation and furthermore, with the balance of energy, to the equation of heat conduction (12.26), which forms a coupled initial boundary value problem with the balance of momentum and the appropriate set of boundary conditions.

$$c_\varepsilon\left(\boldsymbol{\varepsilon}^e,\theta,\boldsymbol{\alpha}\right)\dot{\theta}=\theta\,\frac{\partial^2\psi}{\partial\theta\partial\boldsymbol{\varepsilon}^e}\cdot\dot{\boldsymbol{\varepsilon}}^e+\frac{1}{\rho}\boldsymbol{\sigma}\cdot\boldsymbol{\varepsilon}^i-\frac{\partial}{\partial\boldsymbol{\alpha}}\left(\psi+\theta\eta\right)\cdot\dot{\boldsymbol{\alpha}}-\frac{1}{\rho_R}\,\mathrm{div}\,\mathbf{q}+r \tag{12.26}$$

In (12.26), the heat capacity c_ε belongs to the thermodynamic potential ψ and refers to fixed state of deformation. The volumetric heat supply r is negligible for the observed materials.

Work ratios dating back to the pioneering findings of TAYLOR/QUINNEY, 1934, are used to give insight into the material behaviour. Additionally, the ratio φ (resp. "ETR" in **Fig. 12.8**) of the corresponding rates assesses the kinetics on the energetic level along the load path and provides, therefore, even more information with respect to the chosen material model.

$$e_i=\frac{1}{\rho}\boldsymbol{\sigma}\cdot\dot{\boldsymbol{\varepsilon}}^i\quad\text{and}\quad e_s=\frac{\partial\hat{\Psi}}{\partial\boldsymbol{\alpha}}\dot{\boldsymbol{\alpha}}\quad\text{combined to}\quad\varphi:=e_s/e_i \tag{12.27}$$

The generalised understanding of mechanical deformation as a thermomechanical process can be connected to all sorts of possible deformation mechanisms and their analytical representation. In the last decades, numerous contributions investigated the mechanical deformation behaviour, with reference to plasticity or viscoplasticity (replacing the index "i" by either "p" or "vp" in the equations above).

The presented results of the thermomechanical analyses focus on metal alloys, where the experimental findings for a copper alloy suggest a viscoplastic behaviour (Sparr et al., 2020). In this case, the thermomechanical analysis adopts two significantly different material models for viscoplastic deformation phenomena. The first viscoplasticity model by Bodner and Lindenfeld (1995) is slightly extended in the description of the hardening behaviour, which has been outlined in 12.2.3.2, but maintains it overall structure. It is again emphasised that it does not apply a yield limit. The plastic strain rate is proportional to the stress deviator and its kinetics is

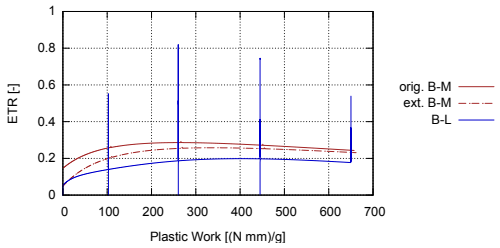

Fig. 12.8 Tensile test with stepwise increased strain rate – ETR–Plastic Work curve.

represented in the proportionality factor by an exponential function. The negative exponent itself contains the hardening parameters and is limited by the stress deviator. The saturation behaviour in the hardening range is accounted for through the plastic stress power in the evolutionary equations, which is also the regulatory entity for the consistent thermomechanical coupling.

The second model proposed by Bröcker and Matzenmiller (2013) is based on rheological model principles and returns to the strict separation of pure elastic and elastic-viscoplastic deformation with a classical yield function, which is the core of the PERZYNA rule of viscoplasticity. The hardening variables obey simple evolution equations and account for the typical saturation behaviour. The original model was extended to account for viscous deformation below the yield limit. For both cases, the reader is referred to the original articles and the given sources therein.

In the context of finite deformation, a more generalized approach was given by Shutov and Ihlemann (2011). The presented framework is a more detailed additive split of the HELMHOLTZ free energy by adding an energy fraction, which "… stands for the remaining part of the energy storage on the microstructural level … [and] is not directly connected to any hardening effects".

A second investigation was directed at an additive manufactured stainless steel. The Ultrafuse 316L filament from BASF is well suited for 3D printing on typical FDM 3D printers. After printing, the tensile testing samples are subjected to a standard MIM (Metal Injection Molding) rinsing and a sintering processes to obtain the final shape (Form E2 $\times$ 6 $\times$ 25 according to DIN 50125). In this case, a classical elasto-plastic material model is applied. Its motivation, mathematical formulation and the thermomechanical consistency are thoroughly discussed in Kamlah and Haupt (1998).

The basic ingredients for the stress-strain characteristic are the VON MISES type yield function:

$$f = \sqrt{\frac{2}{3}\left(\boldsymbol{\sigma}-\boldsymbol{\xi}\right)' \cdot \left(\boldsymbol{\sigma}-\boldsymbol{\xi}\right)'} - \sigma^{y} \tag{12.28}$$

and an associated flow rule. The symbol $()'$ expresses the deviatoric part of the tensorial entity, where the back stress and the yield limit are identified by $\boldsymbol{\xi}$ and by σ^{y}, respectively. Here, the analysis for this material model is restricted to kinematic hardening, where the evolutionary equation for the back stress follows the FREDERICK-ARMSTRONG type:

$$\dot{\boldsymbol{\xi}} = c\dot{\boldsymbol{\varepsilon}}^{p} - \frac{\dot{s}b}{1+ap}\boldsymbol{\xi}. \tag{12.29}$$

The material parameters a, b and c are non-negative and the accumulated plastic strain s is calculated from the consistency condition $\dot{f} = 0$. The first order differential equation in Eq. (12.29) is non-linearly coupled with the evolution of the second internal variable p:

$$\dot{p} = \frac{\dot{s}}{s_0}\left(\|\boldsymbol{\xi}\| - p\right) \quad . \tag{12.30}$$

The positive material parameter s_0 reflects the range of cycles, which is necessary to adapt to a new plastic strain amplitude in a cyclic loading regime with the amplitudes being stepwise constant. The proposed model accounts for cyclic hardening as well as cyclic softening. In consequence to the applied stress-like internal variables $\boldsymbol{\xi}$ and p, Kamlah and Haupt (1998) develop the equation of heat conduction by means of the free enthalpy as the corresponding thermodynamic potential. All related equations can be transferred to the potential of the free HELMHOLTZ energy by the LEGENDRE transform.

All models are implemented in the finite element software suite Abaqus FEA as a user subroutine in the one-dimensional representation and are numerically analysed accordingly.

12.3.2 Experimental Approach

Fundamental contributions to the experimental setup were made by Chrysochoos et al. (1989); Rosakis et al. (2000). The technical progress in accuracy (≈ 0.01 K) and resolution (≈ 1 Megapixel) of current infrared (IR) cameras extended the applicability and simplified the experimental setup. By own experiences (Sparr et al., 2020), no extra measures have to be applied to control the thermal boundary conditions. Standardized, blackened, flat copper samples were investigated by using the ImageIR® 8300 camera (InfraTec GmbH, Germany).

Additionally, the IR camera was used as an extensometer. In this regime, a random, high emissive pattern was applied on the surface of the sample. A well-designed correlation algorithm of the IR image sequence combined with an emissivity correction scheme allows an accurate displacement compensation in the temperature measurement as well as a surface strain field evaluation, which meets the accuracy of other contact-free methods.

The temperature evolution of the full specimen surface as well as the temperature of the clamps were established. The machine and the camera were synchronized by a trigger signal.

12.3.3 Results and Discussion

The model parameters were identified by tensile tests at various strain rates. The model was validated by a more complex loading scheme. **Figure 12.9** (*left*) shows the calculated stress-strain curve of four load-unload loops, while the strain rate is increased stepwise. Especially, the unloading slopes are best met by the BODNER-LINDENFELD model (B-L). The temperature evolution is illustrated by **Fig. 12.9** (*right*) and is in good accordance with the measured temperature field.

The graphs in **Fig. 12.8** of the applied models gives a third characteristic - the ratio φ over the plastic work. The final plastic work value after four steps is almost

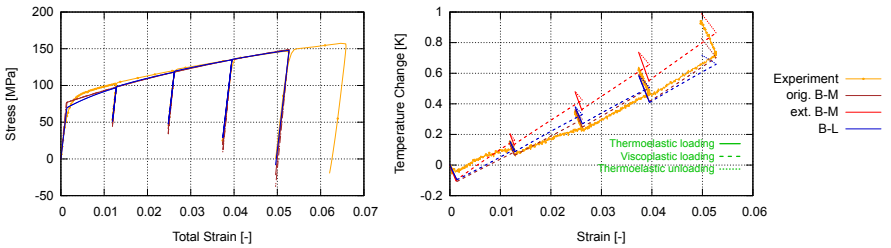

Fig. 12.9: Tensile test with stepwise increased strain rate – (*left*) σ–ε curve and (*right*) ΔT–ε curve.

identical for all three curves, while the values of the ETR ratio for the BRÖCKER-MATZENMILLER models (original resp. extended B-M) are slightly higher than for the B-L model. The starting ETR ratios at the beginning of the elastic-viscoplastic deformation match for the extended B-M and the B-L model only. In contrast to the B-M models, the BODNER-LINDENFELD model shows a very pronounced dynamics in the turning points of the load parameter (transition for loading to unloading and vice versa) .

In the pure tensile test, the elastic-plastic material model by Kamlah and Haupt (1998) is limited to kinematic hardening. The graphs in **Figs. 12.10** and **12.11** compare two parameter sets for the additive manufactured stainless steel. The main differences occur quali- and quantitatively at the beginning of plastic deformation. While the σ-ε curve of set 2 agrees very well with the experimental data (blue),

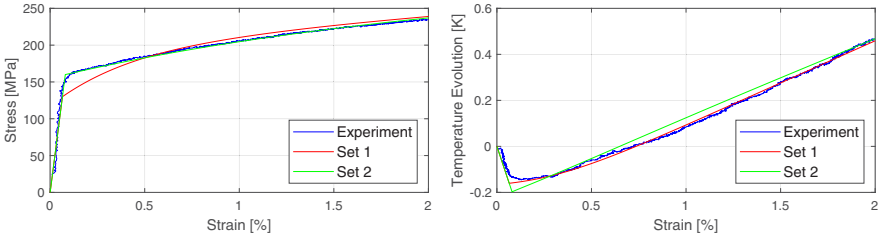

Fig. 12.10: Tensile test stainless steel (AM) with the application of the KAMLAH-HAUPT model – (*left*) σ–ε curve and (*right*) ΔT–ε curve.

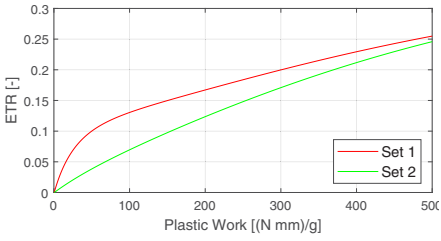

Fig. 12.11 Tensile test stainless steel (AM) with the application of the KAMLAH-HAUPT model – ETR–Plastic Work curve.

the set 1 is better suited to describe the smooth transition at the yield limit in the temperature characteristics.

This becomes even more obvious in the ETR characteristics. The larger slope of the parameter set 1 at the beginning of plastic deformation accommodates better the behaviour observed of other metals or metal alloys, which poses questions on the applied material model. The microstructure of the printed material has significant differences to its casted counterparts in terms of grain size and voids. Therefore, it is sensible to look for theoretical enhancements in the thermomechanical formulation, which reflect the described effects of continuum damage mechanics in Sect. 12.2 for polymers, or to investigate the microstructure of materials with a complex manufacturing procedure in more detail and apply suitable homogenisation strategies. Both approaches rely on the numerical and experimental methods and tools in the macroscopic scale.

12.4 Numerical Models Based on CT Data

While materials with moderate void volume fraction can be modeled with an ansatz from continuum damage mechanics (cf. Sect. 12.2), other microstructures need to be investigated at their corresponding scale. In the case of complex deformation mechanisms of network structures or an unknown multiphase material interaction, **Fig. 12.12**, it is necessary to take the actual microstructure of the material into account. It is important in the description of the material behaviour for numerical analyses. One of the methods of analysing such materials is the preparation of a geometry model and its discretization based on computed tomography (CT) (Richert and Huber, 2018).

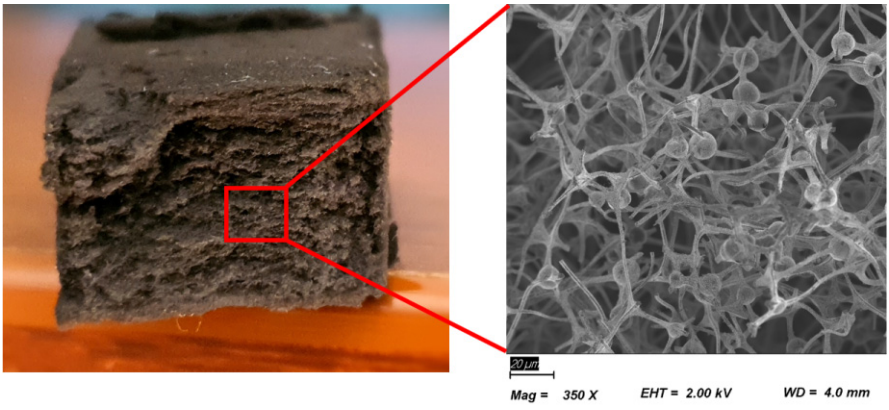

Fig. 12.12: An example of a material with a non-homogeneous microstructure and a microscopic image made with the SEM technique.

Various modelling approaches simplify and parametrise the complex microstructure of porous materials for studying the structure–property relationship based on artificially generated structures. This chapter presents an approach to generate computational efficient and versatile finite element (FE) beam models which are based on skeletonization and diameter information derived from CT data. The geometrical skeleton network is thoroughly examined for a better understanding of the microstructural material behaviour and to define an effective representative volume element (RVE). A skeleton FE beam model is derived that can predict the macroscopic mechanical behaviour of the material (**Fig. 12.13**). Comparisons of the mechanical response between a beam model and a model based on a volumetric discretisation for the skeleton structure are conducted. The skeletonization algorithm was implemented in the open-source software FIJI (Schindelin et al., 2012), among other things commonly used for the geometry analysis and reconstruction of image data.

Based on the imaging process (DICOM), the skeleton is obtained using the FIJI software package. The sequence of grayscale images are thresholded first to obtain binary data. For this purpose, Otsu method (Otsu, 2018) was used. Next, using medial surface axis thinning algorithms (Lee et al., 1994) images of this sequence were skeletonized (**Fig. 12.14**) resulting in a new sequence of images, with white pixels on the estimated axes of beams only. In-house tools, based on the OpenCV library and the Python environment, were then used to create a finite element mesh.

First, the data from Fiji, in the form of a series of monochrome bitmaps, are read. Then, the whole volume is scanned, pixel by pixel, for all x, y and z coordinates, using a frame of the size $3 \times 3 \times 3$ pixels. The further actions will be applied if the central pixel is white, depending on the number of neighbouring white pixels within the frame.

If there is only one neighbouring white pixel, the current pixel is considered as an endpoint. If there are exactly two neighbours, the current pixel lies on the beam. If there are three or more neighbours, the current pixel represents a beam junction (**Fig. 12.15**). Between neighbouring points the linear elements are created, forming an initial mesh. After the scanning of the bitmap series, the initial mesh is being simplified. The endpoint and junction nodes are preserved, while the most of the

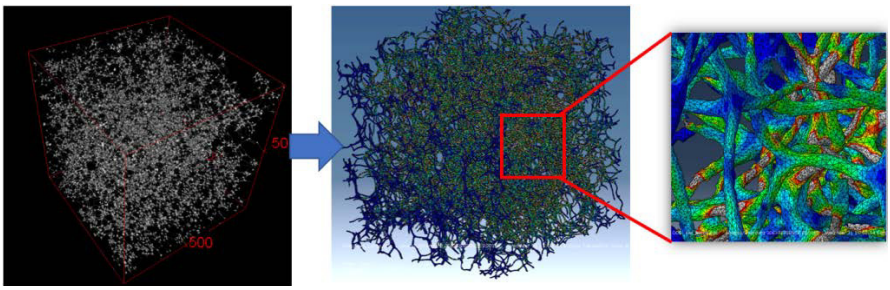

Fig. 12.13: CT model and its representative FE model based on a full geometry volume.

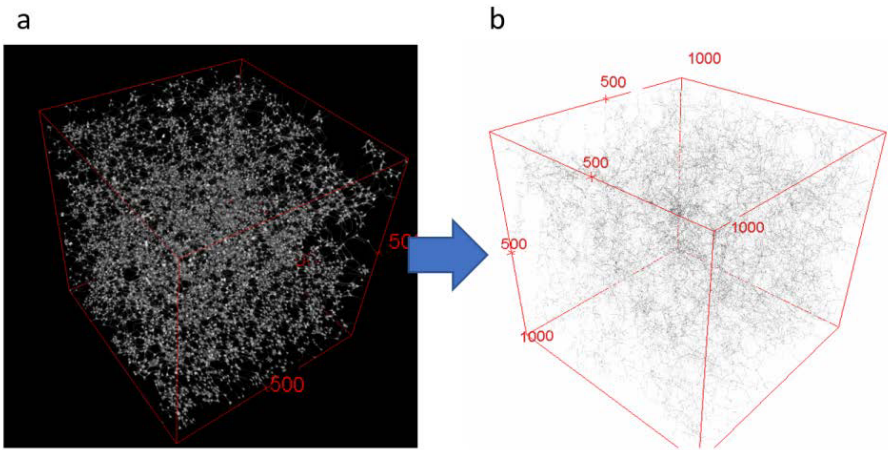

Fig. 12.14: The process of skeletonization from CT data in FIJI software.

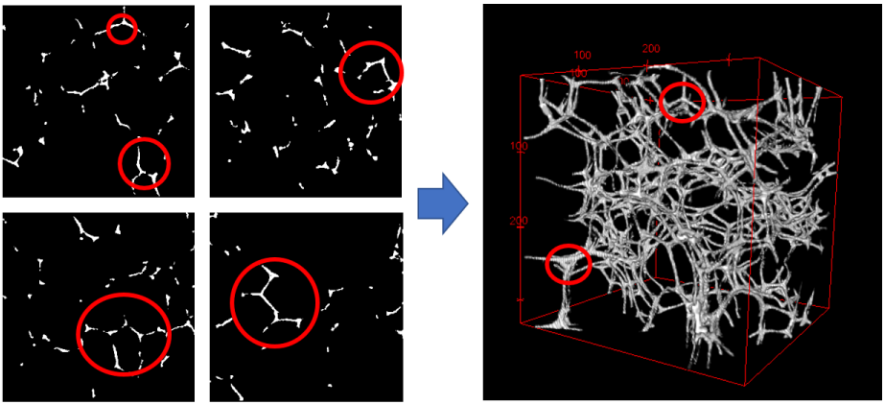

Fig. 12.15: Selected CT imaging sequences and a view of the nodes identifying the connections of individual branches.

rest of the nodes (lying along the beams) are removed. The only exception are nodes lying in the middle of longer beams, which are preserved as well. The same applies to the elements of the initial mesh that connect removed nodes. The next step is the process of filling in the obtained FE model. The Gmsh software will be used for this process. Based on the existing nodes of the skeleton, a mesh is added where matrix properties are assigned to.

The generated FE model incorporates the geometry of the real microstructure and allows for a high computational efficiency (**Fig. 12.16**). To this end, the discretisation of the structure has made use of beam elements available in Abaqus FEA (Abaqus, 2014). As proposed by Huber *et al.*, the cylindrical B31 beam element is used, which account for transverse shear strain in the Timoshenko beam

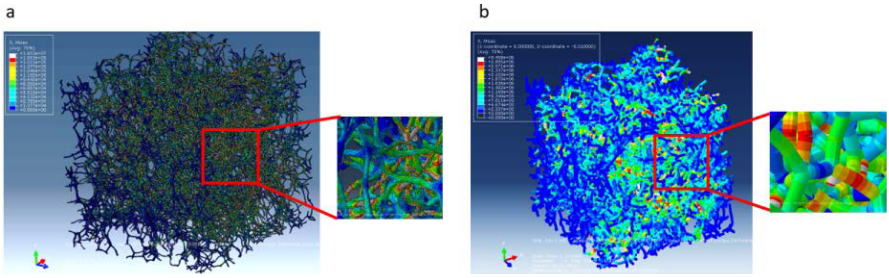

Fig. 12.16: Model comparison: a) FE model based on volumetric elements; b) reduced FE model based on beam elements.

theory (Huber et al., 2014; Roschning and Huber, 2016). In comparison to the artificially generated beam model of Huber *et al.*, the novelty is that the skeleton FE beam model emulates the actual ligament path and shape of the sample, which is based on the skeleton and diameter information, respectively, and extracted from the computed tomography. As for the translation of the tomography data into the beam model, each ligament is divided into several beam elements along the skeleton line. The number of beam elements per ligament depends on the chosen discretisation. Each cylindrical beam element receives the average diameter of the associated voxels. Preliminary numerical validation (**Fig. 12.16**) was performed on the basis of the obtained beam models. The obtained result and the stress concentration in the same computational node were evaluated. The resulting numerical model is useful for creating an effective RVE.

12.5 Summary

Each of the three main sections of this contribution can be considered separately. However, in our understanding, essential points of overlaps exist in the three examined sub-areas of mechanics, so that in the overall view, the combination of the different aspects makes a significant contribution to the analysis of new materials. This concerns both the experimental investigations as well as the numerical simulations.

The temperature dependency of the respective material parameters in Sect. 12.2 is based on the classical decoupling of purely mechanical and purely thermal processes in the context of a continuum mechanical description for the numerical analysis. With the help of experimental observations, a microstructural evolution by nucleation and/or pore growth is proven. This development could be successfully depicted with the integration of continuum mechanical damage models. Slow temperature changes by external heating in a climatic chamber can be adequately represented by the model variants as well, whereby the self-heating due to loading is not accounted for in the material models.

The analytical extension to the full thermomechanical coupling with regard to an evolving temperature field considered in Sect. 12.3 gives additional information about the physicality of the applied material models. The self-heating is driven by the elastic and inelastic deformation and determined by the thermal parameters in the general equation of heat conduction. The temperature evolution is dominated by the internal dissipation and, therefore, strongly related to plastic resp. viscoplastic deformation mechanisms covered in the material models in different ways. The models need to obey to second law of thermodynamics. In addition to the classical stress-strain characteristic, the temperature evolution as well as derived parameters by evaluating of the energy balance are available and complement the physical understanding. The quantification of the dissipation due to damage is currently not taken into account. With respect to damage modeling, additional energy terms according to nucleation and/or pore growth have to be integrated, and the corresponding material parameters have to be quantified.

A similar approach is also conceivable for multiphase materials from complex manufacturing processes. However, the basis for this is an analysis of the components and a microstructural analysis of the interaction of these components. The described image processing and the associated reconstruction algorithms of Sect. 12.4 provide access to a deeper understanding. With the general assumptions of continuum mechanics, the aforementioned methods can be applied on different scales.

Acknowledgements The financial support of the BMWi and AiF Projekt GmbH is gratefully acknowledged.

References

Abaqus (2014) Documentation 6.14. Dassault Systèmes, Providence Road, Rhode Island, USA

Agius D, Kajtaz M, Kourousis KI, Wallbrink C, Wang CH, Hu W, Silva J (2017) Sensitivity and optimisation of the chaboche plasticity model parameters in strain-life fatigue predictions. Materials & Design 118:107–121, DOI 10.1016/j.matdes.2017.01.027

Arndt C, Hauck M, Wacker I, Zeller-Plumhoff B, Rasch F, Taale M, Nia AS, Feng X, Adelung R, Schröder RR, Schütt F, Selhuber-Unkel C (2021) Microengineered hollow graphene tube systems generate conductive hydrogels with extremely low filler concentration. Nano Letters 21(8):3690–3697, DOI 10.1021/acs.nanolett.0c04375, pMID: 33724848

Bodner SR (2000) Unified plasticity - an engineering approach. Final Report for Period 01 AFRL-ML-WP-TR-2001-4019, Technion-Israel Institute of Technology, Haifa 32000, Israel

Bodner SR, Lindenfeld A (1995) Constitutive modelling of the stored energy of cold work under cyclic loading. European Journal of Mechanics - A/Solids 14(3):333–348

Bodner SR, Partom Y (1975) Constitutive equations for elastic-viscoplastic strain-hardening materials. Transaction ASME Journal of Applied Mechanics 42(2):385–389, DOI 10.1115/1.3423586, https://asmedigitalcollection.asme.org/appliedmechanics/article-pdf/42/2/385/5118618/385_1.pdf

Bröcker C, Matzenmiller A (2013) An enhanced concept of rheological models to represent nonlinear thermoviscoplasticity and its energy storage behavior. Continuum Mechanics and Thermodynamics 25(6):749–778, DOI 10.1007/s00161-012-0268-3

Carolan D, Chong H, Ivankovic A, Kinloch A, Taylor A (2015) Co-continuous polymer systems: A numerical investigation. Computational Materials Science 98:24–33, DOI 10.1016/j.commatsci.2014.10.039

Chaboche JL (1989) Constitutive equations for cyclic plasticity and cyclic viscoplasticity. International Journal of Plasticity 5(3):247–302, DOI 10.1016/0749-6419(89)90015-6

Chrysochoos A (2012) Infrared thermography applied to the analysis of material behavior: a brief overview. Quantitative InfraRed Thermography Journal 9(2):193–208, DOI 10.1080/17686733.2012.746069

Chrysochoos A, Maisonneuve O, Martin G, Caumon H, Chezeaux J (1989) Plastic and dissipated work and stored energy. Nuclear Engineering and Design 114(3):323–333, DOI 10.1016/0029-5493(89)90110-6

Cook G, Cook W (1983) A constitutive model and data for metals subjected to large strains, high strain rates and high temperatures. Proceedings of the Seventh International Symposium on Ballistics, The Hague pp 541–547

DIN Deutsches Institut für Normung eV (2012) DIN EN ISO 527-2: Kunststoffe - Bestimmung der Zugeigenschaften: Teil 2: Prüfbedingungen für Form- und Extrusionsmassen

Dupin S, Lame O, Barrès C, Charmeau JY (2012) Microstructural origin of physical and mechanical properties of polyamide 12 processed by laser sintering. European Polymer Journal 48(9):1611–1621, DOI 10.1016/j.eurpolymj.2012.06.007

El Ghezal M, Doghri I (2018) Porous plasticity: Predictive second moment homogenization models coupled with Gurson's single cavity stress-strain solution. International Journal of Plasticity 108:201–221, DOI 10.1016/j.ijplas.2018.05.006

Forster AM (2015) Materials testing standards for additive manufacturing of polymer materials: State of the art and standards applicability. Nist interagency/internal report (nistir), National Institute of Standards and Technology, Gaithersburg, MD, DOI 10.6028/NIST.IR.8059

Franke R, Schob D, Ziegenhorn M (2017) Prüfverfahren und numerische Simulation von mechanischen Eigenschaften 3D-gedruckter thermoplastischer Kunststoffe, Springer Fachmedien Wiesbaden, pp 137–158. DOI 10.1007/978-3-658-17780-5_9

Gong YP, Hyde CJ, Sun W, Hyde TH (2010) Determination of material properties in the chaboche unified viscoplasticity model. Proceedings of the Institution of Mechanical Engineers, Part L: Journal of Materials: Design and Applications 224(1):19–29, DOI 10.1243/14644207JMDA273

Goodridge RD, Tuck CJ, Hague RJM (2012) Laser sintering of polyamides and other polymers. Progress in Materials Science 57(2):229–267, DOI 10.1016/j.pmatsci.2011.04.001

Gurson AL (1977) Continuum theory of ductile rupture by void nucleation and growth - Part I. Yield criteria and flow rules for porous ductile media. Journal of Engineering Materials and Technology 99(1):2–15

Haupt P (2002) Continuum Mechanics and Theory of Materials, 2nd edn. Springer-Verlag, DOI 10.1007/978-3-662-04775-0

Huber N, Viswanath R, Mameka N, Markmann J, Weißmüller J (2014) Scaling laws of nanoporous metals under uniaxial compression. Acta Materialia 67:252–265, DOI 10.1016/j.actamat.2013.12.003

Kachanov M (1980) Continuum model of medium with cracks. Journal of the Engineering Mechanics Division 106(5):1039–1051, DOI 10.1061/JMCEA3.0002642

Kamlah M, Haupt P (1998) On the macroscopic description of stored energy and self heating during plastic deformation. International Journal of Plasticity 13(10):893–911, DOI 10.1016/S0749-6419(97)00063-6

Khdir Y, Kanit T, Zaïri F, Naït-Abdelaziz M (2013) Computational homogenization of elastic–plastic composites. International Journal of Solids and Structures 50(18):2829–2835, DOI 10.1016/j.ijsolstr.2013.03.019

Krempl E (1987) Models of viscoplasticity some comments on equilibrium (back) stress and drag stress. Acta Mechanica 69(1):25–42, DOI 10.1007/BF01175712

Lee T, Kashyap R, Chu C (1994) Building skeleton models via 3-d medial surface axis thinning algorithms. Graphical Models and Image Processing 56(6):462 – 478, DOI 10.1006/cgip.1994.1042

Lemaître J, Desmorat R (2005) Engineering Damage Mechanics: Ductile, Creep, Fatigue and Brittle Failures. Springer, Berlin and New York

Oldyrev PP, Tamuzh VP (1969) Energy dissipation in a glass-reinforced plastic during prolonged cyclic deformation. Strength of Materials 1(3):244–248, DOI 10.1007/BF01543209

Olschewski J (1996) Viskoplastische Materialmodellierung und Anwendung im Gasturbinenbau. Technische Mechanik 16(1):39–50

Otsu N (2018) A threshold selection method from gray-level histograms. IEEE Transactions on Systems, Man, and Cybernetics 9(1):62 – 66, DOI 10.1109/TSMC.1979.4310076

Perzyna P (1963) The constitutive equations for rate sensitive plastic materials. Quarterly of Applied Mathematics 20:321–332, DOI 10.1090/qam/144536

Reese S (1998) Multiplicative thermo-viscoplasticity: A thermodynamic model and its finite element implementation. Technische Mechanik 18(3):209–216

Rice J, Tracey D (1969) On the ductile enlargement of voids in triaxial stress fields. Journal of the Mechanics and Physics of Solids 17(3):201–217, DOI 10.1016/0022-5096(69)90033-7

Richert C, Huber N (2018) Skeletonization, geometrical analysis, and finite element modeling of nanoporous gold based on 3d tomography data. Metals 8(282):1 – 20, DOI 10.3390/met8040282

Rosakis P, Rosakis A, Ravichandran G, Hodowany J (2000) A thermodynamic internal variable model for the partition of plastic work into heat and stored energy in metals. Journal of the Mechanics and Physics of Solids 48(3):581–607, DOI 10.1016/S0022-5096(99)00048-4

Roschning B, Huber N (2016) Scaling laws of nanoporous gold under uniaxial compression: Effects of structural disorder on the solid fraction, elastic poisson's ratio, young's modulus and yield strength. Journal of the Mechanics and Physics of Solids 92:55–71, DOI 10.1016/j.jmps.2016.02.018

Schindelin J, Argenda-Carreras I, Frise E (2012) Fiji: an open-source platform for biological-image analysis. Nature Methods 9:676 – 682, DOI 10.1038/nmeth.2019

Schob D, Roszak R, Sagradov I, Sparr H, Ziegenhorn M, Kupsch A, Léonard F, Müller BR, Bruno G (2019) Experimental and numerical simulation of material and damage behaviour of 3D printed polyamide 12 under quasi-static loading. Archives of Mechanics 71(4-5):507–526, DOI 10.24423/aom.3162

Schob D, Sagradov I, Roszak R, Sparr H, Ziegenhorn M, Kupsch A, Léonard F, Müller B, Bruno G (2020) Experimental determination and numerical simulation of material and damage behaviour of 3D printed polyamide 12 under cyclic loading. Engineering Fracture Mechanics 229(106841), DOI 10.1016/j.engfracmech.2019.106841

Shutov AV, Ihlemann J (2011) On the simulation of plastic forming under consideration of thermal effects. Materialwissenschaft und Werkstofftechnik 42(7):632–638, DOI 10.1002/mawe.201100821

Soyarslan C, Pradas M, Bargmann S (2019) Effective elastic properties of 3d stochastic bicontinuous composites. Mechanics of Materials 137:103,098, DOI 10.1016/j.mechmat.2019.103098

Sparr H, Roszak R, Sagradov I, Schob D, Ziegenhorn M (2020) Thermo-viscoplastic material modelling for self-heating loads and its experimental verification. Technische Mechanik 40(1):66–76, DOI 10.24352/UB.OVGU-2020-015

Stichel T, Frick T, Laumer T, Tenner F, Hausotte T, Merklein M, Schmidt M (2017) A round robin study for selective laser sintering of polyamide 12: Microstructural origin of the mechanical properties. Optics & Laser Technology 89:31–40, DOI 10.1016/j.optlastec.2016.09.042

Taylor G, Quinney H (1934) The latent energy remaining in a metal after cold working. Proceedings of the Royal Society of London Series A, Containing Papers of a Mathematical and Physical Character 143(849):307–326

Truesdell C, Noll W (1992) The Non-Linear Field Theories of Mechanics, 3rd edn. Springer-Verlag, Berlin, DOI 10.1007/978-3-662-10388-3

Tvergaard V, Needleman A (1984) Analysis of the cup cone fracture in a round tensile bar. Acta Metallurgia 32(1):157–169, DOI 10.1016/0001-6160(84)90213-X

van Hooreweder B, de Coninck F, Moens, Boonen R, Sas P (2010) Microstructural characterization of SLS-PA12 specimens under dynamic tension/compression excitation. Polymer Testing 29(3):319–326, DOI 10.1016/j.polymertesting.2009.12.006

Yanase K, Chatterjee H, Ghosh SK (2020) On numerical evaluation of eshelby tensor for superspherical and superellipsoidal inclusions in isotropic elastic material. Composites, Part B 192:107,964, DOI 10.1016/j.compositesb.2020.107964

Zaïri F, Naït-Abdelaziz M, Woznica K, Gloaguen JM (2005) Constitutive equations for the viscoplastic-damage behaviour of a rubber-modified polymer. European Journal of Mechanics - A/Solids 24(1):169–182, DOI 10.1016/j.euromechsol.2004.11.003